NRL Memorandum Report 5647

PHAZR: A Phenomenological Code for Holeboring in Air

J. M. PICONE, J. P. BORIS, M. LAMPE,* AND K. KAILASANATH

Laboratory for Computational Physics

**Plasma Theory Branch*
Plasma Physics Division

September 25, 1985

This work was supported by the Defense Advanced Research Projects Agency under ARPA Order Number 4395 Amendment No. 41.

NAVAL RESEARCH LABORATORY
Washington, D.C.

A159 401

SECURITY CLASSIFICATION OF THIS PAGE

REPORT DOCUMENTATION PAGE

1a REPORT SECURITY CLASSIFICATION UNCLASSIFIED	1b RESTRICTIVE MARKINGS
2a SECURITY CLASSIFICATION AUTHORITY	3 DISTRIBUTION / AVAILABILITY OF REPORT Approved for public release; distribution unlimited.
2b DECLASSIFICATION / DOWNGRADING SCHEDULE	
4 PERFORMING ORGANIZATION REPORT NUMBER(S) NRL Memorandum Report 5647	5. MONITORING ORGANIZATION REPORT NUMBER(S)
6a. NAME OF PERFORMING ORGANIZATION Naval Research Laboratory 6b OFFICE SYMBOL (If applicable) Code 4040	7a. NAME OF MONITORING ORGANIZATION Naval Surface Weapons Center
6c. ADDRESS (City, State, and ZIP Code) Washington, DC 20375-5000	7b. ADDRESS (City, State, and ZIP Code) Silver Spring, MD 20910
8a. NAME OF FUNDING / SPONSORING ORGANIZATION DARPA 8b. OFFICE SYMBOL (If applicable)	9. PROCUREMENT INSTRUMENT IDENTIFICATION NUMBER
8c. ADDRESS (City, State, and ZIP Code) Arlington, VA 22209	10. SOURCE OF FUNDING NUMBERS PROGRAM ELEMENT NO. 62707E; PROJECT NO. WR-W0131; TASK NO.; WORK UNIT ACCESSION NO. DN680-298

11 TITLE (Include Security Classification)
PHAZR: A Phenomenological Code for Holeboring in Air

12 PERSONAL AUTHOR(S)
Picone, J.M., Boris, J.P., Lampe, M. and Kailasanath, K.

13a. TYPE OF REPORT	13b. TIME COVERED	14. DATE OF REPORT (Year, Month, Day)	15. PAGE COUNT
Interim	FROM _____ TO _____	1985 September 25	57

16 SUPPLEMENTARY NOTATION This work was supported by the Defense Advanced Research Projects Agency under ARPA Order Number 4395 Amendment No. 41.

17 COSATI CODES		
FIELD	GROUP	SUB-GROUP

18. SUBJECT TERMS (Continue on reverse if necessary and identify by block number)
Holeboring; Electric discharges; Subgrid turbulence; Charged particle beams; Lasers

19 ABSTRACT (Continue on reverse if necessary and identify by block number)

This report describes a new code for studying holeboring by a charged particle beam, laser, or electric discharge in a gas. The coordinates which parameterize the channel are radial displacement (r) from the channel axis and distance (z) along the channel axis from the energy source. The code is primarily "phenomenological"; that is, we use closed solutions of simple models in order to represent many of the effects which are important in holeboring. The numerical simplicity which we gain from the use of these solutions enables us to estimate the structure of channel over long propagation distances while using a minimum of computer time. This feature makes PHAZR a useful code for those studying and designing future systems.

Of particular interest is the design and implementation of the subgrid turbulence model required to compute the enhanced channel cooling caused by asymmetry-driven turbulence. The approximate equations of Boris and Picone form the basis of the model which includes the effects of turbulent diffusion and fluid transport on the turbulent field itself as well as on the channel parameters.

(Continues)

20 DISTRIBUTION / AVAILABILITY OF ABSTRACT ☒ UNCLASSIFIED/UNLIMITED ☐ SAME AS RPT ☐ DTIC USERS	21 ABSTRACT SECURITY CLASSIFICATION UNCLASSIFIED
22a NAME OF RESPONSIBLE INDIVIDUAL J. M. Picone	22b TELEPHONE (Include Area Code) (202) 767-6326; 22c. OFFICE SYMBOL Code 4040

DD FORM 1473, 84 MAR 83 APR edition may be used until exhausted.
All other editions are obsolete.

SECURITY CLASSIFICATION OF THIS PAGE

19. ABSTRACT (Continued)

The primary emphasis here is on charged particle beams, and as an example, we present typical results for an ETA-like beam propagating in air. These calculations demonstrate how PHAZR may be used to investigate accelerator parameter space and to isolate the important physical parameters which determine the holeboring properties of a given system. The comparison with two-dimensional calculations provide a calibration of the subgrid turbulence model.

CONTENTS

I. INTRODUCTION 1

II. GENERAL STRUCTURE OF THE CODE 4

III. DEPOSITION OF ENERGY 8

IV. THERMAL CONDUCTION 13

V. FLUID TRANSPORT ALGORITHM 15

VI. SUBGRID TURBULENCE MODEL 17

VII. NUMERICAL TESTS AND SIMULATIONS 26

VIII. SUMMARY 28

IX. ACKNOWLEDGMENTS 28

APPENDIX A — A Simple Circuit Model for Energy Deposition in the Atmosphere by an Electron Beam 36

APPENDIX B 42

REFERENCES 51

PHAZR: A Phenomenological Code for Holeboring in Air

I. Introduction

This report describes a new code for studying holeboring by a charged particle beam, laser, or electric discharge in a gas. The coordinates which parameterize the channel are radial displacement (r) from the channel axis and distance (z) along the channel axis from the energy source, hence the letters "ZR" in the name. The code is primarily "phenomenological"; that is, we use closed solutions of simple models in order to represent many of the effects which are important in holeboring. In the case of a particle beam propagating through a gas, we use a model provided by Lee and Buchanan [17] to account for changes in the area of energy deposition (beam radius) with distance from the accelerator. We have modified the treatment of scattering of the beam by the ambient medium to include the results of Hughes and Godfrey [18], as shown in Appendix B. To represent hydrodynamic expansion of the gas heated by a given energy pulse, we use the adiabatic equation of state, which Lampe et al. have shown to be a good approximation [1-3]. The equations of Picone and Boris [4] form the basis of a subgrid turbulence model required to compute the enhanced channel cooling caused by asymmetry-driven turbulence. The numerical simplicity which we gain from the use of such solutions enables us to estimate the structure of a channel while using a far less computer time than a more "detailed" code which solves differential equations for the fields, beam envelope, and the chemistry and dynamics of the ambient gas. This feature permits the computation of channel properties over long propagation distances (e.g., the distance over which significant beam expansion occurs) and thus makes PHAZR a useful code for those studying and designing future systems.

Manuscript approved June 13, 1985.

As indicated by the report title, we have been interested primarily in air, although the model will apply to any chemically nonreactive gas and can be modified to include the effects of chemical reactions. Conversely, the various modules comprising the code can be incorporated easily into other codes. To account for the effects of air chemistry in PHAZR, we currently use a real air equation of state routine based on the equilibrium data of Gilmore [5-6], which cover a temperature range of at least 300 - 24000 K. Using a fast table lookup routine developed by Young [7], we are able to obtain values of γ, the ratio of principal specific heats, over the entire grid in roughly the same amount of time required to compute a vector square root function on the Texas Instruments Advanced Scientific Computer at NRL.

From this discussion, we see that the name PHAZR forms an acronym for "Phenomenological Holeboring in Air using (Z, R) coordinates". In the remaining sections, we discuss the various modules in the code in greater detail. The primary emphasis of this report will be charged particle beams, and as an example, we present typical results for an ETA-like beam propagating in air. These calculations will clearly demonstrate how PHAZR may be used to investigate accelerator parameter space and to isolate the important physical parameters which determine the holeboring properties of a given system.

We note that the subgrid turbulence model is of particular interest because of two features:

(1) This model represents our first attempt at a systematic application of the analysis of asymmetry-generated turbulence to a numerical model of channel physics.

(2) We provide a link between the theory of Boris and Picone, which deals with the generation of large scale turbulent structure (vorticity) and the experimental data of Greig et al. [11], in which the cascade to small scales has taken place.

The problem of multipulse energy deposition leads naturally to a representation in which the effective turbulent diffusivity varies with position in the interior of the channel, since the pulses most likely will not be collinear. Certainly more turbulent transport will occur near the paths of the pulses than in portions of the channel which do not contain the trajectory of at least one pulse. In addition fluid dynamic and turbulent transport will affect the distribution of turbulence and the spatial variation of the turbulent diffusivity within the channel. The model in this report has the above properties and should provide a useful starting point for future treatments of asymmetry - generated turbulence.

II. General Structure of the Code

Because we assume that a given beam, discharge, or laser channel is locally cylindrically symmetric, we use only the radial (r) and axial (z) coordinates. For this discussion we assume that we have a model with closed solutions or tabulated data to describe energy deposition as a function of axial position (z) and time. Appendix B gives an example of such a model [17] for a particle beam. The most important beam parameters for energy deposition at a given z are pulse radius and length and average particle energy, all of which we may estimate from a model or data, which depend mainly on local ambient conditions at the time a pulse propagates past a given point and not on subsequent channel evolution. In order to compute the local conditions for each beam pulse, we need to perform calculations of channel expansion only on transverse slices of the channel which are displaced in z by distances that are small compared to the shortest scale of variation of the beam parameters given above. For example, for a particle beam in a gas, the Nordsieck length normally defines the shortest scale on which the beam pulse expands, and we would choose our slices at intervals of some fraction of the Nordsieck length. The code, therefore, is something less than two dimensional, since the numerical grid consists of a number of weakly connected radial grids, each at a different value of z.

For a given slice (transverse plane) of the channel and a given pulse, the calculation proceeds as shown in Fig. 1. In this paragraph, we will briefly discuss each box. The numbers correspond to those in Fig. 1.

(1) We now consider a string of N pulses and a set of J "channel slices" or planes transverse to the path of propagation, along which energy is deposited in the ambient medium. We compute the channel properties consecutively, beginning with pulse 1 and slice 1, after the ambient values have been entered during initialization. For a given pulse "n", we proceed to each channel slice "j", computing the evolution of the channel up to the time at which another pulse is to be produced by the accelerator.

(2) When we begin a new pulse n, the simulated time elapsed since the passage of the first pulse through slice j is (n-1) times the pulse repetition interval (PRI). Note that the time step number "i" may be different for each slice, since the time step size is determined by local conditions.

(3) Fetch the values of the necessary variables (density, grid cell positions, temperature, ratio of specific heats, and vorticity) from memory for slice j.

(4) From the vorticity ω_i , we compute the turbulent diffusivity α_{Ti} and then a turbulent thermal conduction coefficient λ_{Ti}. We then add λ_{Ti} to the classical molecular thermal conductivity λ_{mi} based on kinetic theory [8,9] to obtain a total effective thermal conduction coefficient λ_i. From the temperature and the ratio of specific heats, we compute the energy density at each radial grid point.

(5) Modify the vorticity distribution based on the turbulent diffusivity α_{Ti}.

(6) Calculate a time step size based on the timescale of energy transport by the effective thermal conduction computed in (4).

(7) We test to see if we are just beginning the calculation on slice j for pulse n.

(8) If so, we compute the radial distribution of energy deposition by pulse n and add this increment to the existing energy distribution. In the case of a particle or laser beam, this step includes the beam dynamics, which determines the radius of energy deposition as a function of propagation distance (slice number). This factor provides a physical link between successive slices along the propagation path.

(9) If the test in (7) is positive, we also compute the increment in vorticity caused by pulse n, but we do not yet update the vorticity distribution.

(10) We modify the energy distribution based on the effective thermal conduction which we calculated in step (4).

(11) The thermal conduction process and the periodic energy deposition by beam pulses, laser pulses, or discharges, cause a departure from pressure equilibrium in this (time-step-split) algorithm. We return to pressure equilibrium in one time step by using the adiabatic equation of state, $P = A \rho^{\gamma}$, where P is the pressure, ρ is the mass density, γ is the ratio of principal specific heats and A is a constant. This equilibration results in the transporting of mass, energy, and vorticity in a Lagrangian manner. This transport will be largest when a new pulse propagates through the slice (i.e., t = (n-1) PRI).

(12)-(13) If this is the first time step for pulse n (t = (n-1) PRI),

add the increment in vorticity computed in (9) to the total vorticity. We do this after the fluid transport step (11) above, since the vorticity increment which we compute is the value present after the hot gas has reached pressure equilibrium.

(14) Update the time.

(15) Perform diagnostics.

(16)-(18) When a time interval equal to the PRI has passed, store all of the primary variables (see (3)) and increase the slice index by one.

(19)-(20) When all J slices have existed for a relative time interval n x PRI, we begin the sequence for a new pulse, starting at slice 1, which is nearest the accelerator.

(21) When all pulses have propagated, stop.

In the remaining sections, we present the equations underlying the sequence of steps listed above. The groupings around which the paper is organized are as follows: energy deposition, thermal conduction, fluid transport, and subgrid turbulence. The section on thermal conduction includes a discussion of the time step calculation, and that on subgrid turbulence includes various aspects of vorticity generation and evolution.

III. Deposition of Energy

1. Energy Density vs. Radial Distance

Past holeboring calculations have employed a circuit model (Appendix A) for energy deposition. An important problem with circuit models relates to the radial profile of energy deposition. Although Bennett profiles with different characteristic radii for direct and ohmic contribution will often provide a useful representation, detailed models like VIPER [15] are more realistic. Furthermore, we must account for the decrease in particle energy and the increase in beam radius with increasing propagation distance, as well as the variation of energy deposition and net current with the local density at a given position along the beam path. Constructing and using a table of ohmic and direct energies versus these parameters would entail too much expense and operational difficulty relative to the accuracy which we would expect from the overall model.

We therefore combine the best features of "detailed" models and circuit models by using the following scheme:

(1) For a short distance from the accelerator (~1 m), use a "first principles" code like VIPER to compute tables of direct and ohmic energy density vs. radial displacement from the beam axis vs. local mass density.

(2) At farther distances $z > 1$ m along the beam path, use the local average mass density to compute a corresponding net current from the Viper data and then compute the average beam radius $a(z)$, pulse length $L(z)$, and particle energy from a beam dynamics model or data.

(3) Using the local density at $z > 1$ m and the VIPER data corresponding to a 1 m propagation distance, calculate (interpolated) radial distributions of direct and ohmic energy densities, $(\partial \xi_D / \partial V)$ and $(\partial \xi_\Omega / \partial V)$, where $d\xi_D$ denotes the amount of energy deposited through direct collisions within the volume element dV and $d\xi_\Omega$ carries a similar definition for ohmic heating.

(4) Now assume that the energy deposition densities at axial position $z > 1$ m have the forms $f_D(r/a(z))$, and $f_\Omega(r/a(z))$. We may then preserve the shapes of the functions computed in step (3) above while accounting for beam expansion and conserving energy through the transformation

$$\frac{\partial \xi_D}{\partial V}(r', z) \equiv \frac{\partial \xi_D}{\partial V}\left(\frac{a(z)}{a(1)} r, z\right) = \frac{\partial \xi_D}{\partial V}(r, 1)\left[\frac{a^2(1)}{a^2(z)}\right]. \qquad \text{(III.1)}$$

In eq. (III.1), the "1" signifies the first slice (at approximately 1 m), for which we actually have data, and r' is the radial coordinate for the channel slice at z. This gives us the total direct energy deposition per unit length:

$$\frac{\partial \xi_D}{\partial z}(z) = 2\pi \int \frac{\partial \xi_D}{\partial V}(r', z)\, r' dr' = 2\pi \int \frac{\partial \xi_D}{\partial V}(r, 1)\, r\, dr \qquad \text{(III.2)}$$

We use a similar transformation for the density of energy deposited at $z > 1$ m through ohmic heating. Notice that we have not yet accounted for the decrease in pulse length with increasing z.

(5) Scale the direct energy density to account for the decrease in particle energy and pulse length with increasing propagation distance according to eq. (B13), developed in Appendix B from the circuit model

(Appendix A). This gives us

$$\frac{\partial \xi_D}{dV}(r', z) = \frac{\partial \xi}{\partial V}\left(\frac{a(z)}{a(1)} r, z\right) = \frac{\partial \xi_D}{dV}(r, 1)\left[\frac{a^2(1)}{a^2(z)}\right]\left[\frac{L(z)}{L(1)}\right] R(z, 1) \qquad \text{(III.3)}$$

where

$$R(z, 1) = \frac{\left(\frac{\partial \varepsilon}{\partial z}\right)_{D\infty}(\varepsilon(z))}{\left(\frac{\partial \varepsilon}{\partial z}\right)_{D\infty}(\varepsilon(1))} \qquad \text{(III.4)}$$

is the ratio of the respective changes in particle energy per unit path length due to direct deposition (subscript D) in ambient air ($\rho = \rho_\infty$) for particles of energy $\varepsilon(z)$ and $\varepsilon(1)$. In eq. (III.3) L(z) is the pulse length at propagation distance z from the accelerator.

(6) Again using the circuit model, scale the ohmic energy density distribution for the effective inductance according to eqs. (B16) and (B17). This gives us

$$\frac{\partial \xi_\Omega}{dV}(r', z) = \frac{\partial \xi_\Omega}{\partial V}\left(\frac{a(z)}{a(1)} r, z\right) = \frac{\partial \xi_\Omega}{\partial V}(r, 1)\left[\frac{a^2(1)}{a^2(z)}\right] S(z, 1) \qquad \text{(III.5)}$$

where

$$S(z, 1) = \begin{cases} \dfrac{\ln\left(b/a(z)\right)}{\ln\left(b/a(1)\right)}, & a(z) < b \\ 0, & a(z) > b \end{cases} \qquad \text{(III.6)}$$

Here b is the radial distance from the axis of the beam at which the conductivity falls to a negligible value and is assumed to be constant. This will be a useful approximation if the time dependence of the induction reduces the ohmic energy deposition by a constant factor α, as in eq. (A10).

2. Energy Deposition Off Axis

To discuss energy deposition by a pulse having a trajectory which lies off the channel axis, we first must recall that we have tables or equations for energy density (denoted, in this section only, by ξ) deposited versus radial displacement ($\underset{\sim}{r}$) from the center of the pulse ($\underset{\sim}{R}_0$) versus the local mass density (ρ) in the region where energy is being deposited. The usual procedure is then to use the actual local density (and if tables are being used) to interpolate linearly in density to obtain $\xi(\rho)$ versus $(\underset{\sim}{r} - \underset{\sim}{R}_0)$. When $\underset{\sim}{R}_0 \neq \underset{\sim}{0}$, a one-dimensional cylindrical model can only treat energy deposition as occurring in an annulus centered at R_0. Thus we initially treat the table as data on $\xi(\rho)$ versus $(r - R_0)$, that is, with r and R_0 scalar, to interpolate onto our computational grid.

Note, however, that an annulus of characteristic width "a" at some radius $R_0 \neq 0$ will have a greater area than a circle of radius a, on which the tables are based. We must, therefore, renormalize the energy deposited on the grid by the factor

$$R_\xi = \frac{\int_0^\infty \xi(r,\ 0,\ a)\ r\ dr}{\int_0^\infty \xi(r,\ R_0\ ,a)\ r\ dr}, \qquad \text{(III.7)}$$

where r is the radial coordinate, R_0 is the radial coordinate of the center of the latest pulse, and a is the Bennett radius of the pulse. For example, an annular Bennett-like profile

$$f(r,\ R_0,\ a) \equiv \frac{1}{\left[1 - \left(\frac{r-R_0}{a}\right)^2\right]^2}, \qquad \text{(III.8)}$$

gives us

$$R_\xi\ (a,\ R_0) = \left\{1 + \frac{R_0}{a}\left[\frac{\pi}{2} + \tan^{-1}\ \left(\frac{R_0}{a}\right)\right]\right\}^{-1}, \qquad \text{(III.9)}$$

which is always ≤ 1. If the grid is sufficiently extensive, the denominator in eq. (III.7) is approximately equal to the integral of the unrenormalized energy density over the grid. If not, we assume that the energy deposition has the form of eq. (III.8) and use the value given by eq. (III.9).

IV. Thermal Conduction

The only time dependent physical process currently in the code is thermal conduction, since we are primarily interested in the evolution of the channel temperature after expansion to pressure equilibrium. The design of PHAZR assumes that the time scale of the latter process is short compared to the pulse repetition interval and the time scale of thermal conduction. We use the adiabatic equation of state to set the channel density to the hydrodynamically equilibrated value immediately after one time step. Recent calculations using the HINT code [14] have shown that, with a nonequilibrium chemistry and a time dependent fluid transport algorithm, the minimum pulse repetition interval for which pressure equilibrium is reached at the end of each pulse is approximately 50 μs. This value is also the effective minimum for which turbulence would have any effect on an ETA or ATA beam of ten pulses. Thus PHAZR appears to be useful for estimating the effects of turbulence on channel temperature in most experiments.

Our thermal conductivity is the sum of two terms: a coefficient of molecular thermal conduction, computed from kinetic theory, and an effective coefficient of turbulent thermal conduction λ_T, computed as described in section VI. The coefficient of molecular thermal conduction is [8]

$$\lambda_m = C_e \lambda^0 \tag{IV.1}$$

where

$$\lambda^0 = \frac{8.322 \times 10^3}{\sigma^2 \Omega^*(T^*)} \left(\frac{T}{M}\right)^{1/2} \quad [\text{erg}/(\text{cm s K})] \tag{IV.2}$$

and the Eucken coefficient is [9]

$$C_e = 0.115 + 0.354 \left(\frac{\gamma}{\gamma-1}\right) \tag{IV.3}$$

In eq. (IV.2), σ is the collision diameter associated with air; Ω^* is a normalized collision integral; M is the molecular weight of air; T is temperature in K; and T^* is a normalized temperature. In eq. (IV.3), γ is the ratio of principal specific heats.

Given the total coefficient of thermal conductivity $\lambda \equiv \lambda_m + \lambda_T$, we solve the diffusion equation,

$$\frac{\partial \xi}{\partial t} = \underset{\sim}{\nabla} \cdot \lambda \underset{\sim}{\nabla} T \qquad \text{(IV.4)}$$

explicitly using cell-centered differences, where ξ is the internal energy density. The choice of the timestep is consistent with the criterion of Richtmyer and Morton [10] in order to maintain the stability of the scheme. In fact we use the somewhat more stringent condition

$$\Delta t = 0.25 \min \{N_i k A_i \Delta r_i / \lambda_i C_i (\gamma_i - 1)\}. \qquad \text{(IV.5)}$$

In eq. (IV.5), we are taking the minimum of the quantity in brackets over the grid, where N_i is the particle density in cell i, A_i is the area enclosed by cell i, Δr_i is the width, C_i is the circumference of a circle passing through the cell center, and λ_i is the thermal conductivity. The quantity in brackets is approximately the time required for thermal conduction to smooth out a temperature gradient across a given cell.

V. Fluid Transport Algorithm

As stated in the previous section, we are primarly interested in channel evolution after pressure equilibrium has been reached following the passage of a pulse through a given slice of the channel. In particular, PHAZR is applicable to multipulse beams with a pulse repetition interval of approximately 50 μs or greater. Thus we need only use adiabatic expansion to estimate the change in channel properties when a new pulse has propagated through the channel. Over the time scale of channel expansion to hydrodynamic pressure equilibrium, we assume that turbulent energy transport has very little effect. That is, the time scales of energy transport by turbulence and molecular thermal conduction are much longer. Therefore, we allow hydrodynamic equilibration to be instantaneous. The vorticity distribution changes due to this hydrodynamic transport, as well as energy and mass density. After pressure equilibration occurs, only the turbulent velocity field remains. Since we use an effective diffusivity (thermal conductivity) to model the turbulence field and because the internal energy density is much greater than the kinetic energy density, we may eliminate the calculation of radial velocities. The expansion of the channel is Lagrangian, giving us

$$A_i^f = A_i^0 \, (P_i/P_a)^{1/\gamma} \qquad (V.1)$$

where P_i is the pressure prior to transport, P_a is the ambient pressure, A_i is cell area, superscript zero (0) indicates the value just before transport and superscript f indicates the value just after transport. The pressure P_i is the sum of the ambient pressure and the incremental changes in pressure resulting from energy deposition by a pulse and from thermal conduction.

Notice that at the end of each time step, the pressure is always equal to the ambient value. Past calculations with flux corrected transport have shown that deviations from ambient pressure are a few percent after the shock from the most recent pulse has decoupled from the channel. To compute the new internal energy, we derive a value of gamma from a table of data measured by Gilmore [7,8] and use the equation

$$\xi = P_a/(\gamma - 1) \tag{V.2}$$

The mass density is given by the (constant) mass in a cell divided by the new cell volume. Finally we must compute a new value for the vorticity in each cell, according to the equation

$$\omega_{zi}^{f} = \omega_{zi}^{0} \; \rho_i^{f}/\rho_i^{0}, \tag{V.3}$$

Where ω_z is the z-component of the vorticity vector $\underset{\sim}{\omega}$ and i labels the computational grid cells. This vorticity expansion term does not include the effects of diffusive processes, which are also present in the form of the effective thermal conductivity. We discuss diffusive processes in the next section.

VI. Subgrid Turbulence Model

1. Experimental and Theoretical Background

The experiments of Greig et al. [11] have provided strong evidence that any asymmetries in energy distribution by an electric discharge, laser pulse, or particle beam propagating in a gas will lead to an enhancemant of two or more orders of magnitude in the cooling rate of the resulting channel. Schlieren photographs of laser and electric discharge channels [11] indicate that the rapid cooling is related to turbulence, and as the channels cool, self-similar expansion occurs according to the simple empirical equation

$$R^2(t) = R^2(\tau) + 4\alpha\,(t - \tau) \qquad \text{(VI.1)}$$

where R(t) is the radius of the channel, t is the time measured from the instant at which energy deposition begins, τ is the time at which expansion to pressure equilibrium is complete, and α (assumed to be spatially nonvarying in the channel) is an effective thermal diffusivity. Experiments show the diffusivity to be approximately constant for a significant period of time. This behavior would result from the random walk of vortex filaments whose strengths do not decay rapidly.

The fact that an effective diffusivity provides a useful model of the turbulent transport of energy indicates that a subgrid turbulence model should be sufficiently accurate for numerical holeboring codes. In addition, we note that the details of the turbulent structure (spatial distribution of different scale lengths) must not be of major importance, since such information would probably not lead to a spatially constant diffusivity. The size of the region in which the turbulence is generated should, however,

appear in the calculation. We point out that this scale may differ from the channel size and that the turbulent diffusion may, therefore not initially operate evenly throughcut the channel cross section.

A realistic subgrid model should also provide for the evolution with time of the turbulent flow and the effective turbulent diffusivity in accordance with the equation for the evoluton of the vorticity field,

$$\frac{d\omega_z}{dt} = \alpha \nabla^2 \omega_z \, . \qquad \text{(VI.2)}$$

Since our calculation uses time step splitting to treat fluid transport and thermal conduction, we satisfy eq. (VI.2) in two steps:

(1) On the fluid transport step, treat the vorticity as a conserved Lagrangian variable, satisfying the continuity equation just as the mass density does [see eq. (V.3)].

(2) Use the effective total diffusivity α to diffuse the vorticity. We may then use the updated vorticity to define an updated effective turbulent diffusivity and an updated total thermal conductivity. We describe the relationships between these quantities below.

Picone and Boris [4] have developed a detailed theory of vorticity generation by asymmetric energy deposition in a gaseous medium. The important asymmetry types which the theory treats include the following:

(1) Noncollinear pulses or misalignment of an existing channel and a given pulse,

(2) A pulse with a noncircular cross section,

(3) Three dimensional asymmetries leading to energy deposition along a curved axis, and

(4) Fluctuations or nonuniformitites in the energy contours within a pulse. An excellent example of case (4) is the existence of hot spots within a laser pulse due to the presence of several modes [11].

The generation of vorticity follows the equation

$$\frac{d\underset{\sim}{\omega}}{dt} + \underset{\sim}{\omega}\,\underset{\sim}{\nabla}\cdot\underset{\sim}{v} = \underset{\sim}{\omega}\cdot\underset{\sim}{\nabla}\,\underset{\sim}{v} + (\underset{\sim}{\nabla}\rho \times \underset{\sim}{\nabla}P)/\rho^2 \qquad \text{(VI.3)}$$

where $\underset{\sim}{v}$ is the fluid velocity and P is the pressure. Any deviation from cylindrical symmetry will lead to the misalignment of the gradients in pressure and density as the hot channel gas expands to pressure equilibrium with the ambient gas. The source term in eq. (VI.3) will be nonzero, leading to the formation of at least one vortex filament pair, although cases (2) - (4) will lead to more complex vorticity distributions. The strength (or circulation) κ has the form

$$\kappa_{i\beta} = U_m\,[R(\tau) - R(0)]\,\ln\left(\rho_1/\rho(\tau)\right)\,f_{i\beta} \qquad \text{(VI.4)}$$

where i labels the asymmetry class, β labels the vector component, $U_m(\sim c_s)$ is a characteristic velocity of expansion, ρ_1 is the local mass density prior to energy deposition by a pulse, $\rho(\tau)$ the density at the position of the center of the pulse after pressure equilibration, and $f_{i\beta}$ is a form factor usually $\lesssim 1$. For the two-dimensional asymmetries [classes (1), (2), and (4)], the form factor $f_{i\beta}$ is non-negligible only for $\beta = z$, for which the vorticity vector is parallel to the channel axis. Although the form factor is supposedly calculable for the cases of practical interest, experimental pulses and discharges most likely contain some combination which would be difficult to discern and measure. For this reason, we use eq. (VI. 3) with $f_{i\beta}$ varying over a reasonable range of values and calibrate the model with detailed two-dimensional calculations employing FAST2D [4].

These FAST2D calculations involve the solution of the inviscid equations for conservation of mass, momentum, and energy, and include no effective diffusivity. Thus, in two dimensions we resolve the actual asymmetry-induced large scale turbulent structure (vortex filament pairs).

2. Theoretical Effective Diffusivity in the Region of a Vortex Pair

We must now relate the vortex strength to the effective diffusivity. The theory of Picone and Boris shows that asymmetric energy deposition produces one or more vortex pairs. The vortices in each pair have a separation given approximately by the scale length of the local asymmetry which generated the pair. To obtain an effective diffusivity in the region containing a given vortex pair, we assume that a rapid cascade to small scale structure occurs. This is reasonable given the experimental data and the proven viability of an effective constant diffusivity.

Conventional wisdom often presented in conjunction with dimensional analysis states that most of the energy resides in the large eddy scales while the dissipation occurs at the smallest eddy scales. We infer that the flux of fluid through the region originally containing a vortex pair will be constant after the cascade to smaller scales occurs. The smaller eddies will, however, mix the cooler ambient gas being pulled into the channel with the hot channel gas much more effectively than would the original vortex pair driving the flow.

To derive a relationship between α and κ, we consider fig. 2, in which a pair of oppositely directed vortex filaments of radius R_v and strength $\pm |\kappa|$ are contained in a cylindrical region of radius S. We denote the separation of the vortex centers by 2δ. The y-axis is the line passing through the vortex centers, and the x-axis lies midway between the vortices. The fluid velocity along the x-axis is [4]

$$v_x (x,0) = |\kappa| \delta/\pi(x^2 + \delta^2). \qquad \text{(VI.5)}$$

The rate (per unit vortex filament length) at which ambient gas flows into the region of radius S and between the vortices is

$$\frac{\partial^2 M}{\partial t \partial z} \approx \rho_a \int_{-(\delta-R_v)}^{\delta-R_v} dy \quad v_x(0,0) \sim \rho_a |\kappa| 2(\delta-R)/\pi\delta, \qquad \text{(VI.6)}$$

where M is mass and we have assumed that the flow is nonnegligible only outside the radii of the vortices. Numerical simulations [4] have indicated that the value of R_v is approximately $\delta/2$. The mass entrainment rate implied by eq. (VI.1) is

$$\frac{\partial^2 M}{\partial t\, \partial z} = \rho_a \frac{R^2(t) - R^2(\tau)}{t - \tau} = 4\alpha\rho_a. \qquad \text{(VI.7)}$$

Equating the mass entrainment rate of eq. (VI.7) with the large scale flow rate of eq. (VI.6) and setting $R_v = \delta/2$, we obtain

$$\alpha \sim |\kappa|/4\pi \qquad \text{(VI.8)}$$

for the theoretical effective diffusivity α. The turbulent contribution to the thermal conductivity is then [12]

$$\lambda_T \equiv \rho c_p \alpha, \qquad \text{(VI.9)}$$

where c_p is the specific heat when the pressure is constant.

Unfortunately eq. (VI.8) is not yet adequate for our purposes, since the effective diffusivity applies only in the region of the vortex pair or, equivalently, in the region of the nonuniformity which generated the vortex pair. Therefore, we must localize the turbulent transport coefficient within a distance S_i (the scale of the region containing the vortex pair) of the position $\underset{\sim}{R}_i$ of vortex pair i. For example, we may use a step function

$$\alpha_i(r) = \begin{cases} \alpha_i, & |\underset{\sim}{r} - \underset{\sim}{R}_i| < S_i \\ 0, & |\underset{\sim}{r} - \underset{\sim}{R}_i| > S_i \end{cases}, \qquad \text{(VI.10)}$$

where α_i is given by eq. (VI. 8). In the case of PHAZR, we have axisymmetry, so that a pulse which occurs off axis appears as an annulus. Similarly the effective diffusivity resulting from a pulse off axis will be localized in an annular region. To do this, we use a Bennett-like function,

$$\alpha_i(r) = \frac{\alpha_i h_i}{\left[1 + \left(\frac{r - R_i}{S_i}\right)^2\right]^2} \qquad \text{(VI.11)}$$

where r is the radial cylindrical coordinate, R_i is the distance of pulse i from the the origin, and S_i is the scale of the density depression resulting from pulse i. In eq. (VI.11) we have used the factor [see eq. (III.9)]

$$h_i \equiv R_\xi (S_i, R_i) \qquad \text{(VI.12)}$$

to account for the increased area covered by the annulus relative to the original circular region containing the vortex pair. Note that the average of $\alpha_i(r)$ is equal to the effective diffusivity α_i in eq. (VI.8).

3. Model for the Turbulent Field

We now assume that the turbulent velocity field may be approximated by that of a superposition of vortex pairs having a distribution of scale lengths and strengths. Thus we will deal primarily with the vorticity field, the effects of which are being modeled by the turbulent diffusivity. We will assume that pulse "i" has just propagated through a slice of the channel, generating a vortex pair of strength $|\kappa_i|$ given by eq. (VI.4). The scale of the region containing the vortex pair is S_i, which may be estimated from the equation for adiabatic expansion

$$S_i^2 = a_i^2 (P_i/P_a)^{1/\gamma} \quad , \tag{VI.13}$$

where a_i is the radius of energy deposition by pulse i and P_i is the pressure due to rapid, local heating of the channel gas by pulse i. Eq. (VI.10) then gives the contribution of pulse i to the turbulent diffusivity present in the entire beam channel. We convert this to an increment of the total vorticity by multiplying eq. (VI.11) by $4/S_i^2$. This factor comes from first using eq. (VI.8) to convert diffusivity to vortex strength and then dividing vortex strength by the area containing the vortex pair to obtain vorticity (units: s^{-1}). The new total vorticity then becomes

$$\omega\,(r,t_i) = \omega(r,t_i - \Delta t) + 4\,\alpha_i(r)/S_i^2 \tag{VI.14}$$

where $\omega(r,t_i - \Delta t)$ is the vorticity in a slice just prior to the arrival of pulse i. The average diffusivity within the beam channel is then given by the area integral of ω divided by 4π, to be consistent with eq. (VI. 8) and the picture of beam channel turbulence as the superposition of vortex pairs.

Rather than use the average channel diffusivity, we preserve the spatial dependence of the vorticity field by defining the effective channel diffusivity as the product of ω (r,t) and a factor $\langle S \rangle^2/4$. Here $\langle S \rangle$ is an average of the scale sizes $\{S_i\}$ of the vortex pairs generated by the beam pulses. For pulses of the same Bennett radius, we expect $S_i \sim S_j \sim S$ for any two pulses i and j. Thus we have

$$\alpha(r,t_i) \approx S^2 \omega(r,t_i)/4 \qquad \text{(VI.15)}$$

This is consistent with the limiting two-dimensional case shown in fig. 3. Here the pulses are all misaligned and sufficiently distant that the local vorticity is determined by the distance from the nearest vortex pair. We have

$$\omega\ (\underset{\sim}{r},t) \approx \sum_i \omega_i\ (\underset{\sim}{r},\ S_i,\ t) \qquad \text{(VI.16)}$$

where we use the step function of eq. (VI. 10)

$$\omega_i\ (\underset{\sim}{r},\ S_i,\ t) \equiv \begin{cases} 4\alpha_i/S_i^2\ , & |\ \underset{\sim}{r} - \underset{\sim}{r}_i\ | < S_i \\ 0\ , & |\ \underset{\sim}{r} - \underset{\sim}{r}_i\ | > 0 \end{cases} . \qquad \text{(VI.17)}$$

In eq. (VI.17), α_i is the diffusivity in the region of pair i, as given by the integral over the area of that region. The total effective diffusivity is then

$$\frac{1}{4\pi} \int_A \omega(\underset{\sim}{r})\ dA = \frac{1}{4\pi} \sum_i \omega_i(\underset{\sim}{r},\ S_i,\ t)\ \pi S_i^2 = \frac{S^2}{4}\ \omega(\underset{\sim}{r},\ t) \qquad \text{(VI.18)}$$

if the spatial scales $\{S_i\}$ of the vortex pairs are all equal. Equation (VI.15) is therefore consistent with this limiting case.

VII. Numerical Tests and Simulations

We have performed two-dimensional numerical simulations with the code FAST2D [4] to calibrate the results of PHAZR. In both codes, we used a table of data derived from VIPER for energy density deposited versus local mass density. The data correspond to a distance of approximately 1 m from the accelerator nozzle. We assume that the beam parameters are as follows: (1) 10 kA beam current, (2) 5 mm pulse radius, (3) 10 ns pulse length, and (4) 50 MeV beam energy. We used pulse repetition intervals of 1 ms and 100 μs, respectively, and strings of ten pulses. Due to the expense of the two-dimensional simulations, we computed channel properties only in the first channel slice, which was located approximately 1 m from the accelerator nozzle.

The most important difference between the PHAZR and FAST2D calculations is the treatment of the rotational flows generated by asymmetric energy deposition. In the case of FAST2D, the noncollinearity of the pulses generates most of the vorticity and the cascade to smaller scales is restricted by the grid size and the flux-corrected transport algorithm. PHAZR relies on the subgrid turbulence model described in the previous section, and the form factor f in eq. (VI.4) can range from 0.0 (no turbulence) to approximately 1.0 for the cases encountered so far [11,13]. We must, therefore, perform several calculations with PHAZR, each with a different value of f, in order to compare the two models. (We point out that the notation in the figures is "F" instead of "f".)

Figure 4 shows our results for ten pulses with a pulse repetition interval of 100 μs and a range of values for the form factor in PHAZR. Notice that we ran PHAZR calculations for strings of collinear pulses and noncollinear pulses, respectively. Each pulse in the "noncollinear" strings

was displaced from the origin by 0.0, 0.5, or 1.0 times the pulse radius. The FAST2D calculations considered only noncollinear pulses, since in that code no turbulence would be generated in the collinear case. We chose the pulse locations so that a clockwise progression occurred around the first pulse which was centered at the origin. Clearly there are an infinity of patterns from which to choose.

For the 100 μs case, we see that the noncollinearity of the pulses was more important for keeping the channel cool than was turbulence ($f \neq 0$). In addition, turbulence had no apparent effect until the sixth pulse, which occurred at $t = 500$ μs. This is the time scale of the large scale rotational motion [4] and shows that the subgrid turbulence model retains this feature of the motion. Finally we see remarkable agreement between FAST2D and PHAZR when the latter uses a form factor of 0.5.

In fig. 5, we show the results of a similar calculation for a pulse repetition interval of 1 ms. Here turbulence, when compared with noncollinearity, has a larger effect in cooling the channel than for the other case, since the time between pulses (energy depositions) is a factor of ten greater. Once again the PHAZR calculation with $f = 0.5$ gives close agreement with FAST2D.

Figure 6 shows an example of the application of PHAZR. We use the same parameters as above with a pulse repetition interval of 100 μs for a string of 40 pulses. In this case, we have slices at 1, 10, 20, and 30 m from the accelerator and a form factor of 0.5. The time required for the channel to achieve a given temperature increases monotonically with distance from the accelerator. We also see that, because of turbulence, the channel does seem to achieve a somewhat uniform temperature toward the end of the pulse train.

VIII. Summary

For a particle beam accelerator which emits pulses into a gas, PHAZR is useful for estimating channel properties over long distances. PHAZR is also applicable to studies of the cooling of laser or discharge channels. Because this code does not involve the integration of fluid or field equations, the running time is very short, making PHAZR valuable for "systems-level" studies. Calibration of the turbulence model with accurate two-dimensional hydrodynamics simulations has shown excellent agreement, and the initial calculations have shown that pulse-to-pulse noncollinearity can result in a measureably cooler channel, even if turbulence is not significant. We mention that the use of an equilibrium chemistry model and instantaneous deposition could lead to a channel which is too cool, even if there were no shocks to carry energy out of the channel. The trends which the model indicates should, however, be quite useful in assessing channel properties.

IX. Ackowledgments

The authors gratefully acknowledge support for this work by the Defense Advanced Research Projects Agency, ARPA, Order Number 4395, Amendment Number 41. We also appreciate helpful discussions with A.W. Ali, S. Slinker, and E.S. Oran of the Naval Research Laboratory and J. Boyd of Lawrence Livermore Laboratories.

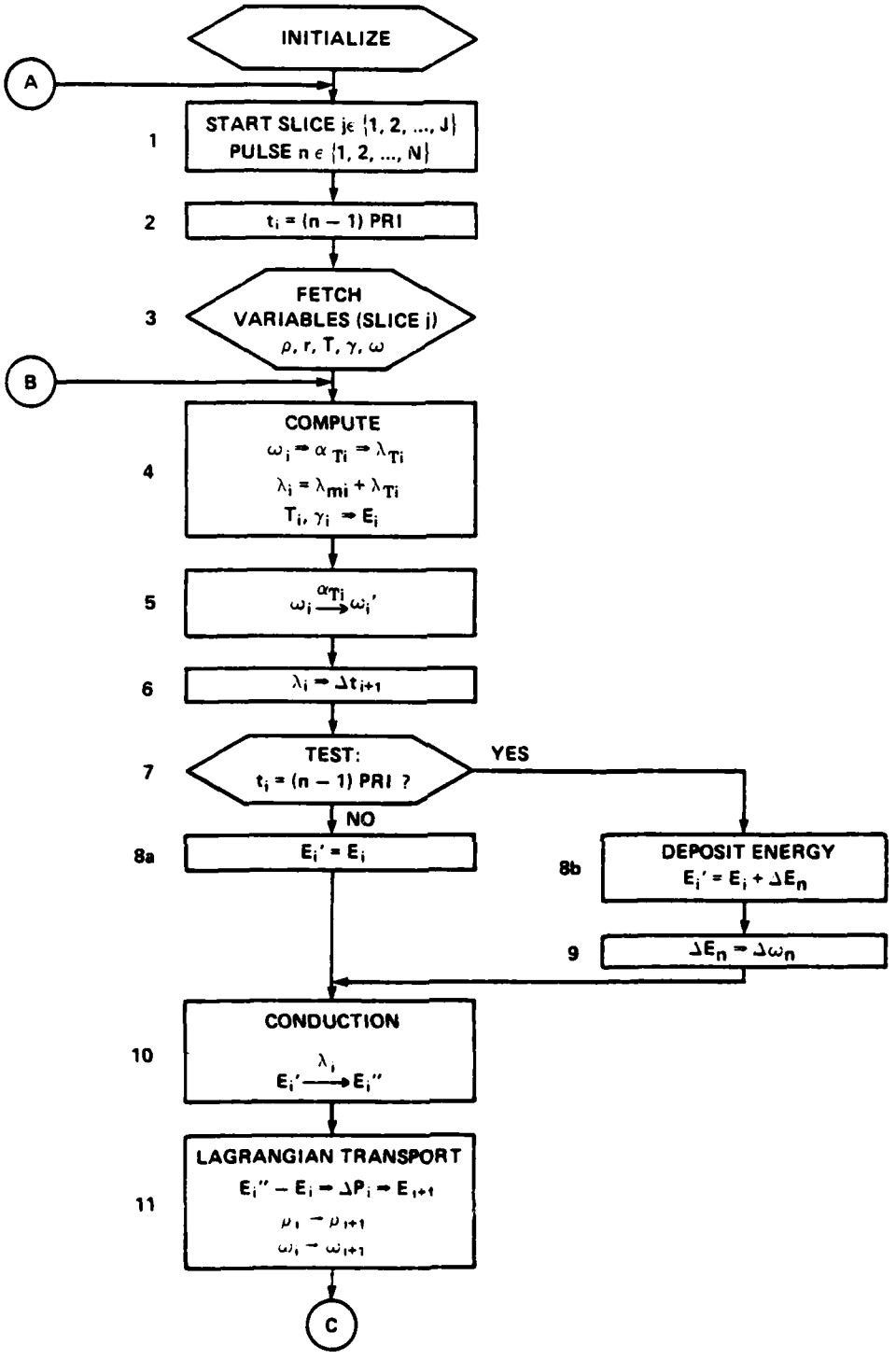

Fig. 1. Flow chart for PHAZR. An expression "A (bold arrow) B" implies that we may derive B from A or "A gives us B". An expression "A ($\xrightarrow{B}$ thin arrow) A'" means that the quantity A is modified in value to A' under the influence of quantity B. The numbers 1-21 beside the boxes correspond to the numbers in section II of the text.

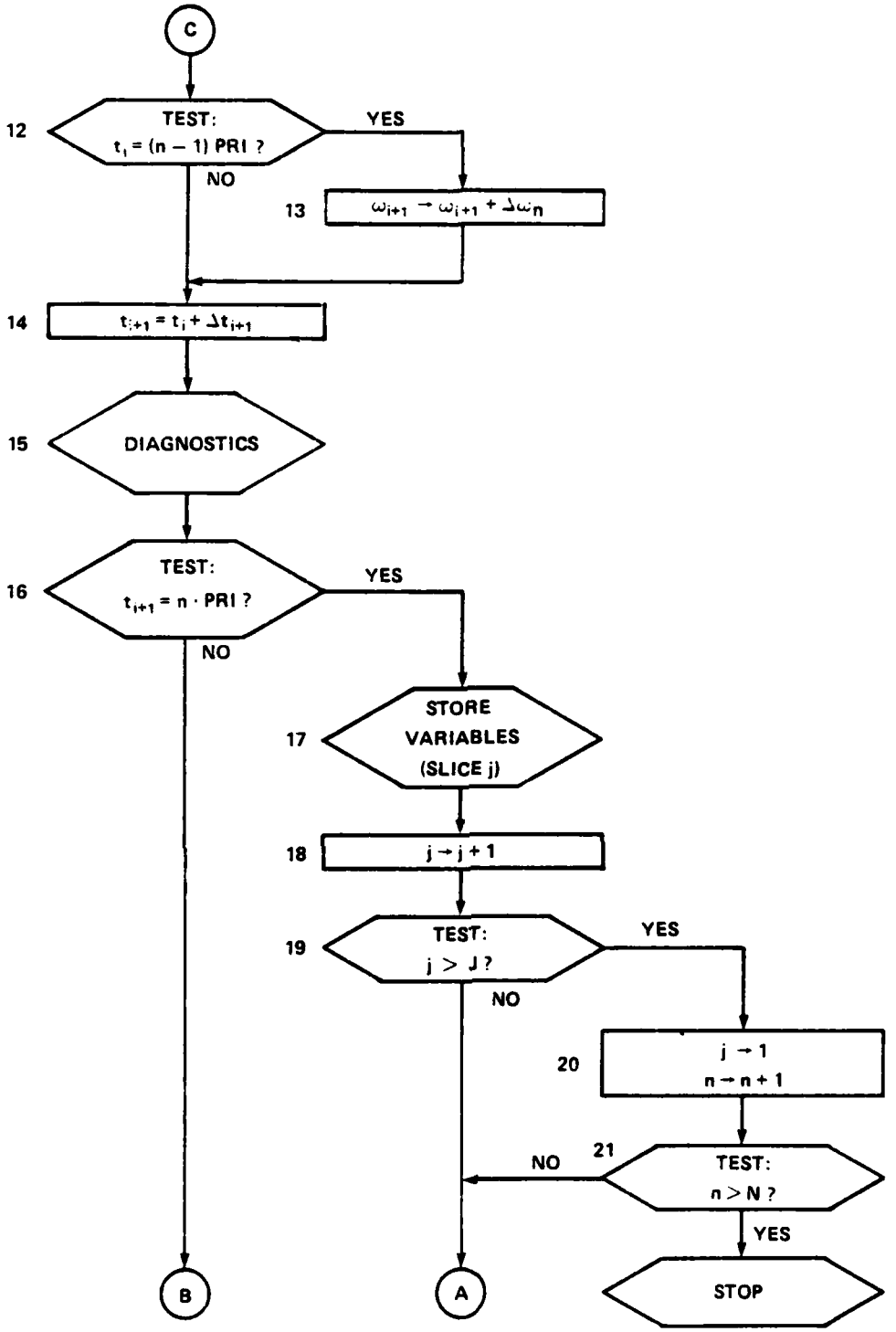

Fig. 1. (con't) Flow chart for PHAZR. An expression "A (bold arrow) B" implies that we may derive B from A or "A gives us B". An expression "A ($\text{thin}^{B}\text{arrow}$) A'" means that the quantity A is modified in value to A' under the influence of quantity B. The numbers 1-21 beside the boxes correspond to the numbers in section II of the text.

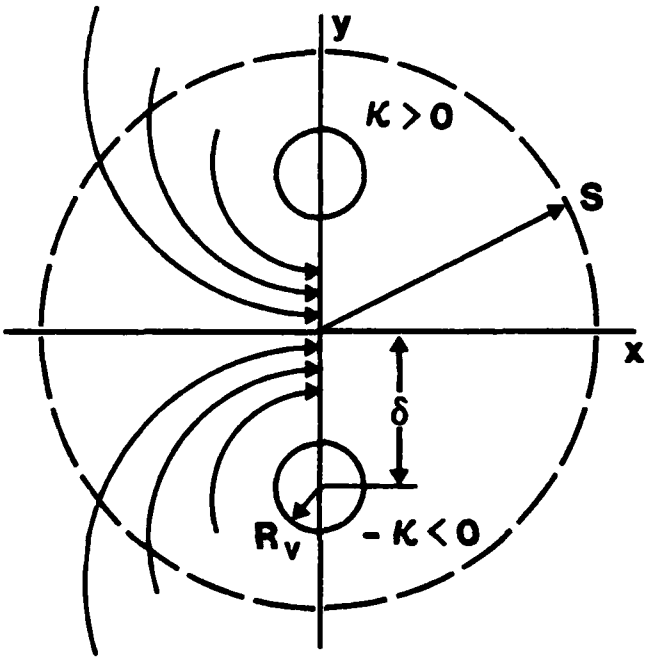

Fig. 2. We define the region of influence of a vortex filament pair by a circle of radius S. The center of the circle forms the origin of our coordinate system. The quantity R_v defines the cross section of each vortex and the separation of the filaments is 2δ. The vorticity vectors of the two filaments are oppositely directed and the quantity κ denotes the magnitude of the strength of each filament.

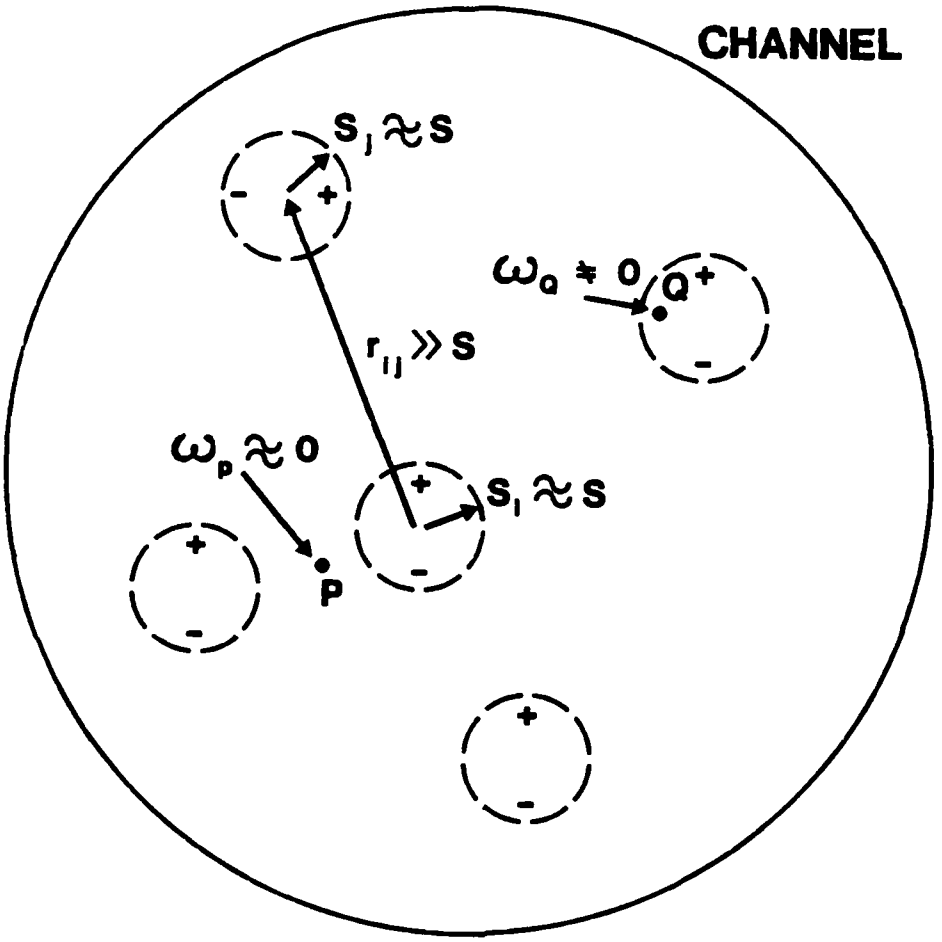

Fig. 3. We consider a channel produced by several pulses which are displaced from each other by a large distance compared to the radii S_i, S_j, etc. In this example, the vorticity is constant and nonnegligible only inside the radius S_i of the ith vortex for all values of E. Since the pulses are all roughly identical, the regions of nonzero vorticity are all of approximately the same size S.

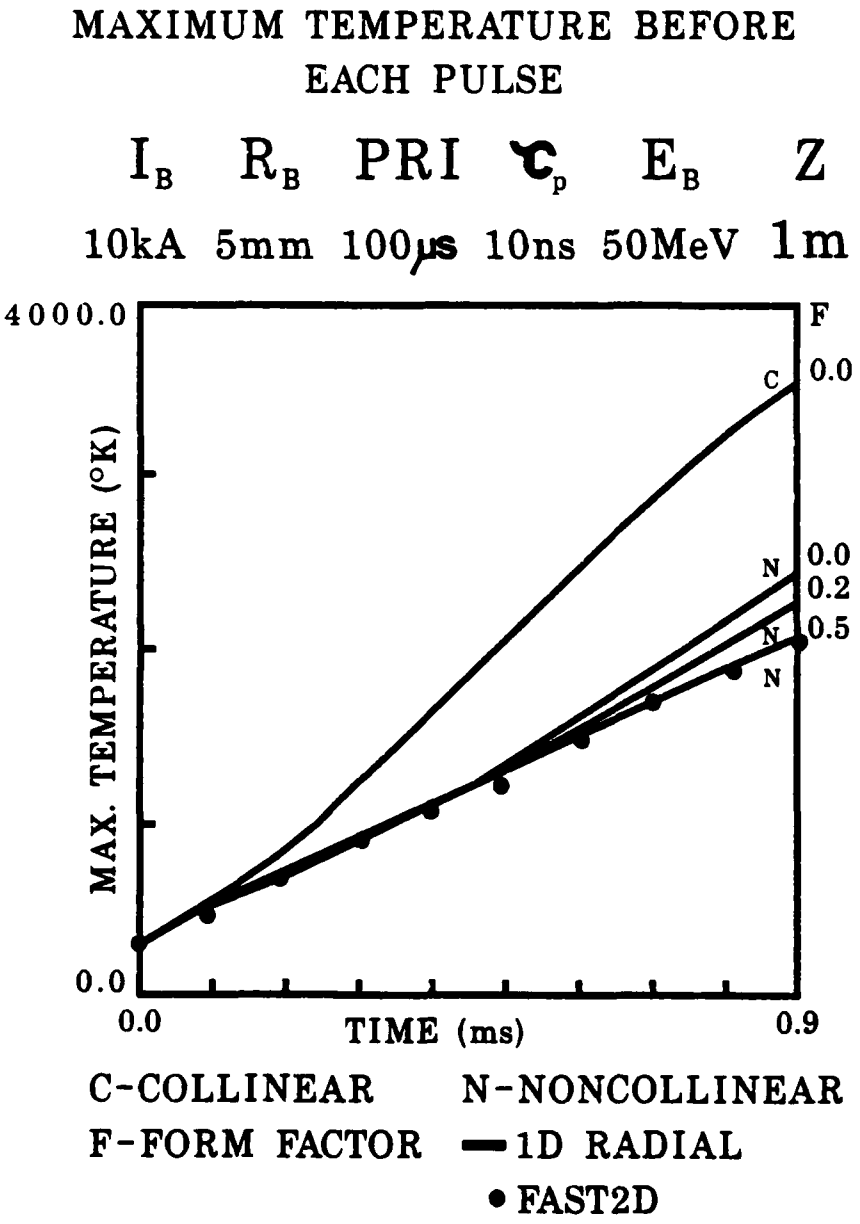

Fig. 4. This figure shows the results of PHAZR and FAST2D calculations of maximum channel temperature just before deposition of energy by each pulse. The beam parameters are given above the diagram. The solid lines give PHAZR plots for different form factors and collinearity properties. The dots are the results of the corresponding FAST2D calculation.

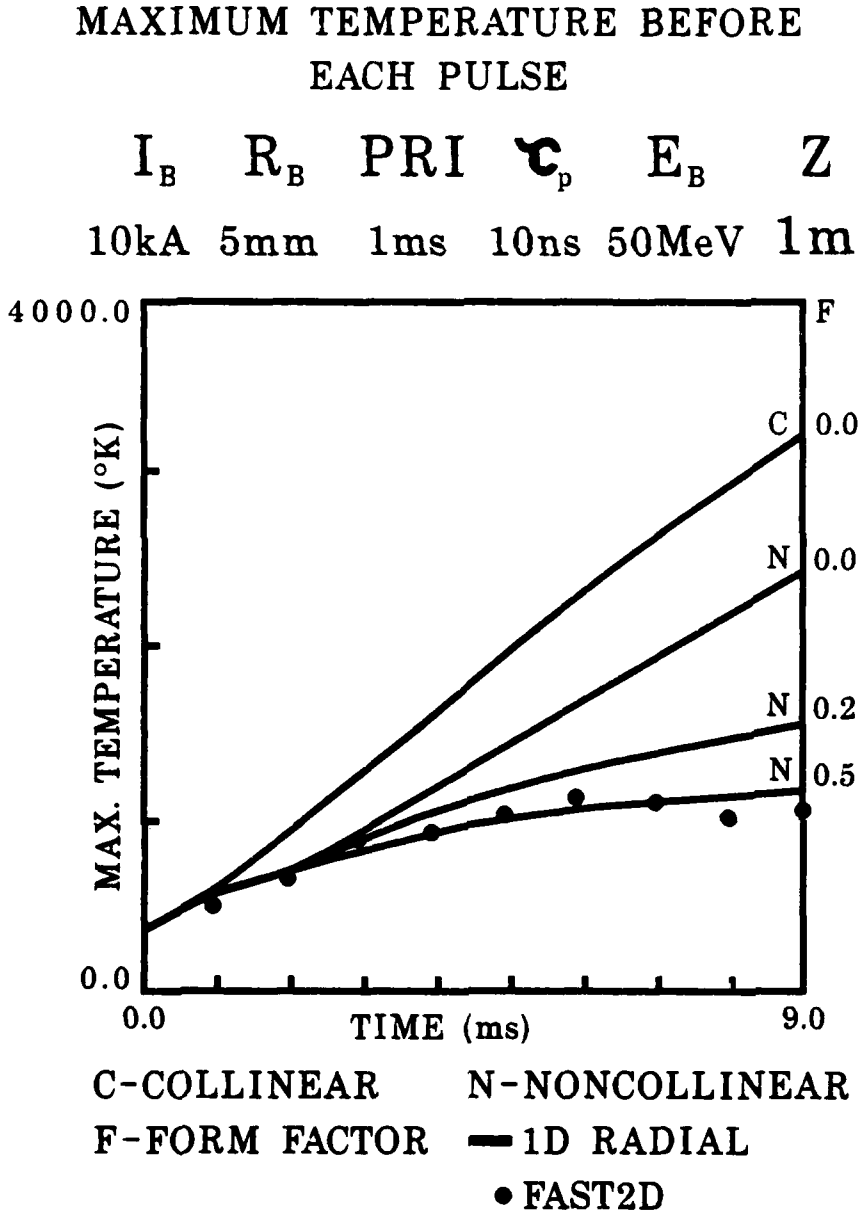

Fig. 5. This figure shows a set of calculations which are similar to fig. 3, except that the pulse repetition interval is 1 ms instead of 100 μs.

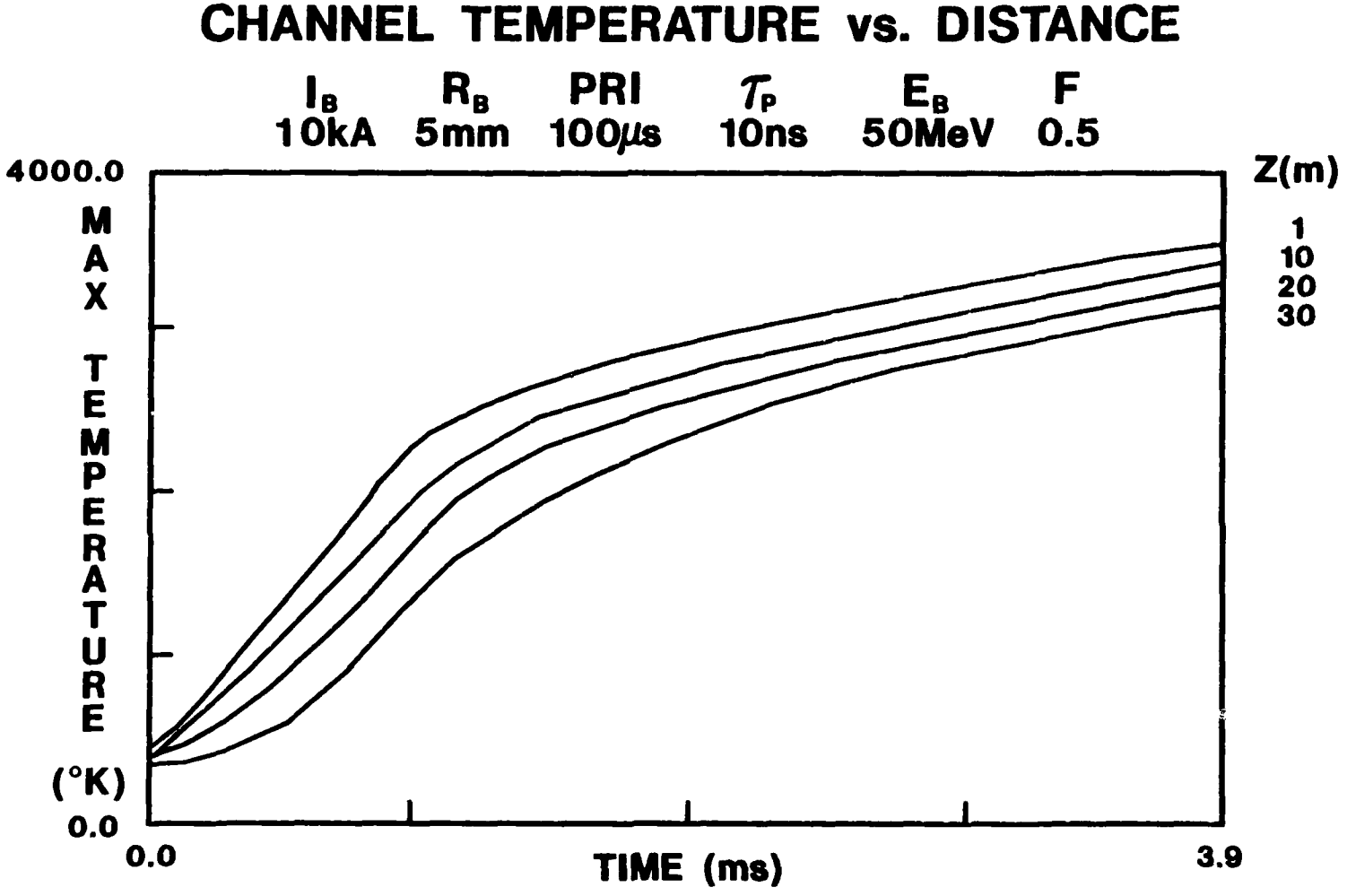

Fig. 6. This figure shows sets of calculations of maximum channel temperature at different values of z, the position along the beam path. Here we have a string of 40 pulses, instead of 10 pulses, as in fig. 3 and 4.

APPENDIX A

A SIMPLE CIRCUIT MODEL FOR ENERGY DEPOSITION IN THE ATMOSPHERE BY AN ELECTRON BEAM

1. Direct Collisions

The average "direct" energy loss rate per electron, per cm of propagation distance is

$$\left(\frac{d\varepsilon}{dz}\right)_D = \frac{\rho}{\rho_\infty} \left(\frac{d\varepsilon}{dz}\right)_{D\infty}, \tag{A1}$$

where z is the distance of the head of the pulse from the source, ρ is the average channel density, ρ_∞ is the ambient density, and the change in particle energy due to direct collisions in full density air is $\left(\frac{d\varepsilon}{dz}\right)_{D\infty} \approx$ 2.5 keV/cm. The subscript "D∞" on the right hand side implies direct collisions (D) in ambient, full density(∞) air. Thus $\left(\frac{d\varepsilon}{dz}\right)_{D\infty}$ acts as an effective electric field, and the energy in joule/cm deposited at z by direct deposition is

$$\frac{d\xi_D}{dz} = I_b \left(\frac{d\varepsilon}{dz}\right)_{D\infty} \tau_p \, \rho/\rho_\infty. \tag{A2}$$

In eq. (A2), ξ_D is the total energy deposited via direct collisions, I_b is the electron beam current in amperes and τ_p is the pulse length in seconds. For simplicity, we may assume that the radial energy distribution has a Bennett profile:

$$\frac{d\xi_D}{dV}(r) = \frac{1}{\pi a_D^2} \frac{d\xi_D}{dz} \Big/ \left(1 + \frac{r^2}{a_D^2}\right)^2, \tag{A3}$$

in which a_D is the Bennett radius and $d\xi_D/dV$ denotes the density of energy deposited through direct collisions. The Bennett radius a_D, for a given beam emittance, depends on the net current I_n, which may be determined by a calculation using the VIPER computer code [15]. The ratio I_n/I_b varies slowly with the position ζ (measured from the front of the pulse), except at the expanded head. Constant average values for a_D and I_n, therefore, provide an adequate representation for the circuit model. For a 10kA beam current, a 10ns pulse length, and ambient density, we find $d\xi_D/dz \approx 0.25$ J/cm, which is comparable to the ohmic deposition, as we shall see below.

2. Ohmic Deposition

As is common with circuit models of beam energy deposition in a gas, we assume that the conductivity σ is high enough that the displacement current can be neglected and that no net (beam and air plasma) charge exists out to radius $b >>$ beam radius a_D. A further assumption is that b is a constant multiple of $a_D(z=0)$. Maxwell's equations (mks units: volts, amperes, meters) then give us

$$\underset{\sim}{\nabla} \times \underset{\sim}{E} = - \frac{\partial \underset{\sim}{B}}{\partial t} \tag{A4}$$

or

$$E_z(r) = - \frac{d}{dt} \int_r^b B_\theta(r')\, dr' \approx - \frac{d}{dt} \int_{a_D}^b B_\theta\,(r')\, dr' \,, \tag{A5}$$

since, for $r < a_D$, $E_z(r)$ is approximately independent of r over the beam cross section (variation $\lesssim$ 20%). We also have

$$(\underset{\sim}{\nabla} \times \underset{\sim}{B})_z = \frac{1}{r} \frac{\partial}{\partial r} r\, B_\theta = \mu_0 J_n \,, \tag{A6}$$

where $\mu_0 = 4\pi \times 10^{-7}$ H/m and J_n is the net current density along the axis of the pulse (z-axis). Equation (A6) results in

$$B_\theta(r) = \frac{\mu_0}{2\pi r} I_n(r) \quad , \tag{A7}$$

where $I_n(r)$ is the net (beam + plasma) current within radius r. For $r \gtrsim a_D$ we have

$$B_\theta(r) \approx \frac{\mu_0}{2\pi r} I_n \tag{A8}$$

in which I_n is the total net current and is independent of r. Using eq. (A8) in eq. (A5), we find that

$$E_z \approx - \frac{\mu_0}{2\pi} \dot{I}_n \ell n \left(\frac{b}{a_D}\right) . \tag{A9}$$

Notice that the factor $(\mu_0/2\pi)\ell n(b/a_D)$ plays the role of an inductance, which is assumed to be constant in most simple circuit models. At the radius b, the conductivity, by definition, becomes too small for the plasma to provide space charge neutralization. For $r > b$, therefore, E_z drops to zero, an assumption which was used implicitly to integrate eq. (A4). A representative value for b is usually around 20 a_D (z=0). Unfortunately calculations using VIPER have indicated that the inductance changes with ζ, leading to a considerable reduction (factor of 2 or 3) in ohmic energy deposition. A crude representation of this would be to multiply eq. (A9) by a Factor $\alpha \equiv 1-f$, where f represents the fractional reduction in

electric field E_z resulting from an inductance which varies with ζ. We might expect α to vary with the density of the gas (pre-existing channel) into which the latest pulse is injected. Thus we have

$$|E_z| \rightarrow \frac{\alpha\mu_0}{2\pi} \dot{I}_n \ell n(b/a_D) \ . \tag{A10}$$

The energy which is extracted from the beam (and eventually deposited in the air) per meter of path traversed is

$$\frac{d\xi_\Omega}{dz} \equiv \int_0^{\tau_p} I_b |E_z| d\tau' , \tag{A11}$$

in which τ_p is the duration of the pulse in seconds and the integration variable τ' is the time since the pulse head traversed a particular point in space. We could alternatively integrate over $\zeta \equiv ct - z$, which gives position in the pulse relative to the beam head.

In keeping with our model of the beam in which each pulse has a constant beam current I_b of duraction τ_p, we neglect the following:
(1) erosion of pulse length, which depends on the propagation range, but is typically only a small fraction of the pulse length;
(2) the rise of I_b at the head (justified after the rising part, typically $\approx$ 0.3ns, has eroded away);
(3) the fall of I_b at the pulse tail, which results in relatively little ohmic energy deposition, since the conductivity σ is high, and E_z is small there.

From eqs. (A10) and (A11), we find that the energy deposited through ohmic heating is

$$\frac{d\xi_\Omega}{dz} = \frac{\alpha\mu_0}{2\pi} \; I_b \; I_n(\tau_p) \; \ell n(b/a_D) \qquad \text{(A12)}$$

The Bennett profile, eq. (A3), provides a less faithful representation of ohmic energy deposition than of direct energy deposition, although past holeboring calculations have used the Bennett profile in the absence of better data. From Viper calculations, we find that the profile for ξ_Ω decreases less rapidly with radius than that for ξ_D. If a Bennett profile is used, we would expect that the Bennett radius a_Ω should be chosen to be greater than a_D. As explained in Section III of this report, we circumvent this problem by retaining the general profile of the VIPER data at all slices along the beam path.

We would expect the above model of ohmic deposition to suffer somewhat from its simplicity. In the beam head, the conductivity is low even within the beam radius. Electrostatic neutralization is incomplete, and radial electrostatic fields and displacement currents exist. A detailed treatment [16], however, gives the same result for ohmic deposition except that I_n is replaced by an effective current I_e, which includes electrostatic effects. At $\tau' = \tau_p$ (the tail of the beam), $I_e = I_n$, and at $\tau' = 0$, $I_e = 0$, so that the integral in eqs. (A11) and (A12) remains the same. We note that much of the energy in eq. (A12) is extracted from the nose of the beam, where the radius is expanded, and electrostatic effects must receive consideration.

The subsequent deposition of this energy in the air occurs primarily through $\underset{\sim}{E} \cdot \underset{\sim}{J}_p$ in the main body of the beam (or even after the beam has passed by a given location), where J_p is the plasma current density. In the body of a pulse, the radius is approximately constant, E_z is relatively independent of r, and J_p has a profile quite similar to that of the beam. This provides some justification for approximating the profile for ohmic deposition by a Bennett profile. Storage of energy in the associated magnetic field causes a delay between extraction of energy from the beam and deposition in the air.

APPENDIX B

In this Appendix, we seek to transform the equations of Lee and Buchanan [17] (below we will designate this reference by "LB") into forms which are compatible with the use of data from calculated by VIPER rather than from a circuit model. From this standpoint, VIPER provides shapes for the direct and ohmic energy deposition and values of $\frac{d\xi_D}{dz}$ and $\frac{d\xi_\Omega}{dz}$, the respective total energies deposited per unit path length.

1. Particle Energy

Denoting the energy per particle in MeV by ε, the equation of LB for the change in particle energy with propagation distance z is

$$\frac{d\varepsilon}{dz} = -\frac{\varepsilon}{\lambda_R} - \left(\frac{d\varepsilon}{dz}\right)_D , \qquad (B1)$$

where λ_R is the "radiation length" and $(d\varepsilon/dz)_D$ is the change in particle energy due to direct deposition (ionization loss rate). We may also define an effective ohmic loss per particle $(de/dz)_\Omega$ by dividing the ohmic loss by the number of particles in a pulse. In eq. (B1), the initial particle energy is $0.511\ \gamma$ (MeV); $\gamma \equiv 1/(1-\beta^2)^{1/2}$; $\beta = v/c$; and v is the average velocity of the beam particles. LB treat λ_R and $\left(\frac{d\varepsilon}{dz}\right)_D$ as constants in integrating eq. (B1). Assuming that these quantities do vary slowly with z, we suggest that simple averages of the values at the limits of integration would be more appropriate. If we integrate eq. (B1) between positions z_i and z_{i+1} along the beam path, we

obtain

$$\varepsilon(z_{i+1}) = \varepsilon(z_i)\ \exp[-(\ z_{i+1} - z_i)/\langle\lambda_R\rangle_{i,\ i+1}]$$

$$- \langle\left(\frac{d\varepsilon}{dz}\right)_D\rangle_{\ i,i+1}\ \langle\lambda_R\rangle_{i,i+1}\left(1- \exp[-(z_{i+1}-z_i)/\langle\lambda_R\rangle_{i,i+1}]\right) \tag{B2}$$

where

$$\langle\lambda_R\rangle_{i,i+1} \equiv 1/2\ \{\lambda_R(z_i) + \lambda_R(z_{i+1})\} \tag{B3}$$

and

$$\langle\left(\frac{d\varepsilon}{dz}\right)_D\rangle_{\ i,i+1} \equiv 1/2\ \{\left(\frac{d\varepsilon}{dz}\right)_D(z_i) + \left(\frac{d\varepsilon}{dz}\right)_D(z_{i+1})\}. \tag{B4}$$

Where no ambiguity is possible, we will drop the subscripts i and i+1 on the average (bracketed) quantities in subsequent equations, and we will denote quantities evaluated at a given position by the corresponding subscript. Our integrals will always occur between positions z_i and z_{i+1}.

We will now express $\left(\frac{d\varepsilon}{dz}\right)_D$ and $\left(\frac{d\varepsilon}{dz}\right)_\Omega$ in terms of $\frac{d\xi_D}{dz}$ and $\frac{d\xi_\Omega}{dz}$, the total direct and ohmic energies, respectively, deposited per unit path length. If N_e is the total number of elections in a beam pulse, we have

$$\frac{d\varepsilon}{dz} = \frac{1}{N_e}\ \frac{d\xi}{dz}\ , \tag{B5}$$

where

$$N_e = n_e \pi a^2{}_D L. \tag{B6}$$

In eq. (B6), L is the pulse length, a_D is the beam radius, and n_e is the average electron density. The beam current is then

$$I_b = n_e e c \pi a_D^2, \tag{B7}$$

in which e is the electron charge and c is the speed of light. Substituting eq. (B7) into eq. (B6), we obtain

$$N_e = \frac{LI_b}{ec} \tag{B8}$$

and

$$\frac{d\varepsilon}{dz} = \frac{ec}{LI_b} \frac{d\xi}{dz} . \tag{B9}$$

To be consistent with LB, we express eq. (B9) in terms of MeV/m, assuming that $\frac{d\xi}{dz}$ is given in erg/cm:

$$\frac{d\varepsilon}{dz} = \frac{d\xi}{dz} \frac{1}{LI_b} \frac{(1.6022 \times 10^{-19}C)(2.9979 \times 10^{8}m/s)(100cm/m)}{(10^{7}erg/J)(1.6022 \times 10^{-19}J/ev)(10^{6}eV/MeV)}$$

$$= \frac{2.9979 \times 10^{-3}}{LI_b} \frac{d\xi}{dz} , \tag{B10}$$

where L is given in m and I_b is the beam current measured in amperes (A). Again to be consistent with LB, we express I_b in terms of the value in kiloamperes (kA) to obtain

$$\frac{d\varepsilon}{dz} \text{ (MeV/m)} = \frac{2.9979 \times 10^{-6}}{LI_b(kA)} \frac{d\xi}{dz} \text{ (erg/cm)} \tag{B11}$$

Equation (B11) applies to both ohmic and direct deposition of energy; however, further discussion of the dependence on pulse length is necessary for

the remaining sections. Both direct and ohmic deposition per electron depend explicitly on L^{-1}. However, the circuit model in Appendix A indicates that $\frac{d\xi_D}{dz} \propto L$ while $\frac{d\xi_\Omega}{dz}$ depends on L mainly through the logarithmic variation of effective inductance with beam radius. Thus $(\frac{d\varepsilon}{dz})_D$ is approximately independent of L while $(\frac{d\varepsilon}{dz})_\Omega$ varies primarily as L^{-1}.

At positions distant from the accelerator nozzle, we may use the circuit model (Appendix A) to modify VIPER data, which give $\frac{d\xi_\Omega}{dz}$ and $\frac{d\xi_D}{dz}$ versus ρ at positions close to the accelerator nozzle. If the first position (i=1) corresponds to the VIPER data, we have from eqs. (A1) and (A2)

$$\frac{d\xi_D}{dz} \propto (\frac{d\varepsilon}{dz})_{D\infty} L, \tag{B12}$$

so that, for position $i > 1$ and a given local channel density ρ,

$$(\frac{d\xi_D}{dz})_i = (\frac{d\xi_D}{dz})_1 \frac{(\frac{d\varepsilon}{dz})_{D\infty\, i}}{(\frac{d\varepsilon}{dz})_{D\infty\, 1}} \frac{L_i}{L_1} \tag{B13}$$

We define

$$R_{i1} \equiv \frac{(\frac{d\varepsilon}{dz})_{D\infty\, i}}{(\frac{d\varepsilon}{dz})_{D\infty\, 1}} \tag{B14}$$

for which approximate values may be obtained from the particle energies, ε_1 and ε_i, corresponding to positions z_1 and $z_i > z_1$. From eqs. (B11) - (B14), we find that

$$(\frac{d\varepsilon}{dz})_{Di} = \frac{2.9979 \times 10^{-6}}{L_1 I_b (kA)} (\frac{d\xi_D}{dz})_1 R_{i1}, \tag{B15}$$

which is indeed independent of pulse length, as we would expect for energy deposition by direct collisions.

For ohmic deposition in air of a given local density ρ, we have eq. (A12)

$$\frac{d\xi}{dz} \propto \ell n\ (b/a_D). \tag{B16}$$

Defining

$$S_{il} \equiv \frac{\ell n(b/a_{Di})}{\ell n(b/a_{Dl})}, \tag{B17}$$

and assuming that b is approximately constant, we have

$$\left(\frac{d\varepsilon}{dz}\right)_{\Omega i} = \frac{2.9979 \times 10^{-6}}{L_i\ I_b(kA)} \left(\frac{d\xi_\Omega}{dz}\right)_l S_{il}. \tag{B18}$$

In the section B.3 we shall see that a_D varies approximately as exp $[A(L_l - L_i)]$, where A is a constant. The quantity S_{il}, therefore, depends only weakly on L, as we would expect.

2. Pulse Length

LB assume that pulse erosion accounts for the effects of ohmic deposition, as well as the other mechanisms summarized by eq. (B1). If we assume that the average number of electrons per unit length, dN_e/dL, is constant in time, we have in the formulation of LB

$$\frac{d}{dz}\,\varepsilon L = -\frac{\varepsilon L}{\lambda_R} - L\left(\frac{d\varepsilon}{\partial z}\right)_D - \Lambda\,\frac{I_n\varepsilon}{I_A}, \tag{B19}$$

in which Λ is the inductance obtained from a circuit model, such as that in Appendix A; I_n (kA) is the net current (beam current + plasma current); and the Alfven current I_A is defined as $1.7\times10^{1}\beta\gamma$(kA) or, equivalently, ε(MeV) times 34(kA/MeV) from LB. As in eq. (B1), LB treat λ_R, $\left(\frac{d\varepsilon}{dz}\right)_D$, and $\Lambda\, I_n\varepsilon/I_A$ as quantities which do not vary with L but which do vary slowly with z. We again suggest replacing them with averages as in eqs. (B2)-(B4). An equivalent equation to eq. (B19) is

$$\frac{d}{dz}\,\varepsilon L = -\frac{\varepsilon L}{\lambda_R} - L\left(\frac{d\varepsilon}{dz}\right)_D - L\left(\frac{d\varepsilon}{\partial z}\right)_\Omega \tag{B20}$$

Comparing (B19) and (B20), we find that

$$\frac{\Lambda I_n\varepsilon}{I_A} \approx \frac{\Lambda I_n}{34} = L\left(\frac{d\varepsilon}{dz}\right)_\Omega . \tag{B21}$$

As noted above, the left hand side of Eq. (B21) does not vary strongly with L and we conclude that neither does the right hand side. Recalling the discussion at the end of section B.1, (eqs. (B12 - B18)) we see that $\left(\frac{d\varepsilon}{dz}\right)_\Omega$ is indeed approximately proportional to L^{-1}, consistent with this conclusion. To obtain the remaining equations which correspond to (B21) from those given by LB, we may therefore replace the quantity $\Lambda I_n/34$ by

$$\langle L\left(\frac{d\varepsilon}{dz}\right)_\Omega \rangle_{i,i+1} = 1/2 \left\{ L_i \left(\frac{d\varepsilon}{dz}\right)_{\Omega i} + L_{i+1} \left(\frac{d\varepsilon}{dz}\right)_{\Omega(i+1)} \right\}, \qquad \text{(B22)}$$

which accounts for the slow z dependence.

From eqs. (B1) and (B19), LB obtain

$$\frac{dL}{dz} = -\frac{\Lambda I_n}{34\varepsilon} = -\frac{L}{\varepsilon}\left(\frac{d\varepsilon}{dz}\right)_\Omega \qquad \text{(B23)}$$

Using eqs. (B1) and (B23), LB also obtain an equation for $dL/d\varepsilon$. From that expression, we obtain the pulse length in eq. (B24):

$$L_{i+1} - L_i = \frac{\langle L\left(\frac{d\varepsilon}{dz}\right)_\Omega \rangle}{\langle \left(\frac{\partial \varepsilon}{\partial z}\right)_D \rangle} \ln \left\{ \frac{\varepsilon_{i+1}}{\varepsilon_i} \left(\frac{\varepsilon_i + \langle \lambda_R \rangle \langle \left(\frac{d\varepsilon}{dz}\right)_D \rangle}{\varepsilon_{i+1} + \langle \lambda_R \rangle \langle \left(\frac{d\varepsilon}{dz}\right)_D \rangle} \right) \right\}. \qquad \text{(B24)}$$

3. Pulse Radius (a)

LB give the Nordsieck equation as

$$\frac{d}{dz} \ln(a\sqrt{\varepsilon I_n}) = \frac{2C_n}{\lambda_R \varepsilon I_n}, \tag{B25}$$

where $C_n \approx 3700$ (MeV - kA). We may make the substitution defined by eq. (B23) in the Nordsieck equation to obtain

$$\frac{d\ \ell n\ (a_D\sqrt{\varepsilon I_n})}{dL} = -\frac{2C_N}{\langle\lambda_R\rangle\ \langle I_n\rangle\varepsilon} \quad (\varepsilon/\langle L(\frac{d\varepsilon}{dz})_\Omega\rangle). \tag{B26}$$

$$\approx -7400/(\langle\lambda_R\rangle\ \langle I_n\rangle\ \langle L(\frac{d\varepsilon}{dz})_\Omega\rangle.$$

Integrating Eq. (B25) between positions z_i and z_{i+1}, we have

$$a_{D(i+1)} = a_{Di}\left(\frac{E_i I_{ni}}{E_{i+1} I_{n(i+1)}}\right)^{1/2} \exp\left\{7400(L_i - L_{i+1})/(\langle\lambda_R\rangle\ \langle I_n\rangle\ \langle L(\frac{d\varepsilon}{\partial z})_\Omega\rangle)\right\} \tag{B27}$$

An alternative form is necessary if we wish to use the expression of Godfrey and Hughes [18] for the Nordsieck length L_N. Here we have

$$L_N = \frac{7.14\ \nu\gamma\ \ln\ (1090\ \nu\gamma)}{[\ln(2970\nu\gamma)]^2}, \tag{B28}$$

where Budker's parameter is defined by

$$\nu = \frac{\gamma I_b}{I_A} \equiv \frac{I_b}{1.7\times10^4\beta}, \tag{B29}$$

in which I is the Alfven current limit and I_b the beam current in amperes (A).

From eq. (B 25), we identify

$$\frac{1}{L_N} \approx \frac{2C_n}{\lambda_R \varepsilon I_n}, \tag{B30}$$

when the work done by the beam varies slowly with propagation distance. Using eqs. (B28) and (B30), we obtain

$$a_{i+1} = a_i \left(\frac{E_i I_{ni}}{E_{i+1} I_{n(i+1)}}\right)^{1/2} \exp[(z_{i+1} - z_i)/L_N]. \qquad \text{(B31)}$$

References

1. M. Lampe, H. H. Szu, and S. Kainer, "Hydrodynamics of Gas Channel Formation," NRL Memo. Rep. 4073 (1979).
2. M. Lampe and S. Kainer, "Gas Channel Formation: Dependence of Hydrodynamic Phenomena on the Initial Radial Pressure Profile," NRL Memo. Rep. 4129 (1979).
3. S. Kainer and M. Lampe, "Gas Channel Formation Studies Including Real-Air Properties," NRL Memo. Rep. 4247 (1980).
4. J. M. Picone and J. P. Boris, Phys. Fluids 26 (2), 365 (1983).
5. F. R. Gilmore, "Equilibrium Composition and Thermodynamic Properties of Air to 24000 K," RAND Corp. Rep. RM-1543 (1955).
6. F. R. Gilmore, "Equilibrium Thermodynamic Properties of High Temperature Air," Lockheed Missile and Space Co. Rep. DASA 1917-1 (1967).
7. T. R. Young, Jr., "Table Look-Up: An Effective Tool on Vector Computers," in Proc. Tenth Conf. Num. Sim. Plasmas (ed. by J. Helton, T. S. Wang, and J. Greene), 3B4 (1983).
8. J. O. Hirschfelder, C. F. Curtiss, and R. B. Bird, Molecular Theory of Gases and Liquids, (John Wiley and Sons, Inc., New York, 1964), 534.
9. J. M. Picone and E. S. Oran, "Approximate Equations for Transport Coefficients of Multicomponent Mixtures of Neutral Gases," NRL Memo. Rep. 4384, 27 (1980).
10. R. D. Richtmyer and K. W. Morton, Difference Methods for Initial-Value Problems (Interscience, New York, 1967), 189.
11. J. R. Greig, R. E. Pechacek, and M. Raleigh, "Channel Cooling by Turbulent Convective Mixing," NRL Memo. Rep. 5280 (1984).
12. G.K. Batchelor, An Introduction to Fluid Dynamics, (Cambridge, New York, 1967), 35.

13. J.M. Picone, J.P. Boris, J.H. Gardner, J.R. Greig, M. Raleigh, M. Lampe, R.E. Pechacek, and R.F. Fernsler in Proceedings of The Fifth International Conference on High Power Particle Beams, ed. by R.J. Briggs and A.J. Toepfer (Lawerence Livermore National Laboratory, Livermore, California, 1984), pp. 378-381.

14. J.M. Picone, A.W. Ali, S. Slinker, J.P. Boris, E.S. Oran, and T.R. Young, Jr., "Multiplulse Holeboring Calculations with Radially Resolved Chemistry," in NRL Memorandum Report 5412, 16 (1984).

15. R.F. Hubbard, M. Lampe, S.P. Slinker, and G. Joyce, "Viper I: A Multicomponent Hose Dynamics Code for Propagating Electron Beams," JAYCOR Tech. Rep. J207-81-005 (1981).

16. W.M. Sharp and M. Lampe, Phys. Fluids 23, 2383 (1980).

17. E.P. Lee and H.L. Buchanan, private communication.

18. T.P. Hughes and B.B. Godfrey, "Improved Treatment of Multiple Scattering of Intense Charged Particle Beams," Mission Research Corp. Rep. AMRC-R-389, 1982.